Nano Research

Open Access

Research Article

Boosted electrosynthesis of hydrogen peroxide on isolated metal sites through second-shell modulation

Hua Zhang[1], Nan Zhang[2], Baojuan Xi[1], Fei Wan[1], Kepeng Song[1], Xuguang An[3], Shenglin Xiong[1], and Xiaogang Li[1] ✉

[1] School of Chemistry and Chemical Engineering, Shandong University, Jinan 250100, China
[2] Shanghai Research Institute of Petrochemical Technology, Shanghai 201208, China
[3] School of Mechanical Engineering, Chengdu University, Chengdu 610106, China

Cite this article: *Nano Research*, **2025**, *18*, 94907211. https://doi.org/10.26599/NR.2025.94907211

ABSTRACT: The electrosynthesis of hydrogen peroxide is limited by the competitive four-electron oxygen reduction reaction (ORR) pathway. The modulation for the adsorption of OOH* intermediate on active sites is considered as the effective approach to tune the ORR selectivity, but it remains challenging. Herein, we report the neighboring phosphorus atom in the second coordination shell to regulate the electronic structure of the isolated Ni-N_4 sites, leading to the favored OOH* adsorption and thus boosting the electrocatalytic ORR to hydrogen peroxide through the two-electron pathway. Spectroscopy characterizations and density functional theory calculations indicate the neighboring phosphorus atom in the second coordination shell triggers the electron transfer to central Ni atom, strengthening the adsorption of OOH* on Ni sites and thus increasing the catalytic performance for two-electron ORR, delivering a selectivity above 90% for production of hydrogen peroxide under the current density of 150 mA·cm^{-2}. This work reveals tailoring second coordination shell of isolated metal sites could be as a precise and efficient way to engineer the catalytic performance, which thus provides a promising approach to the design of advanced catalysts.

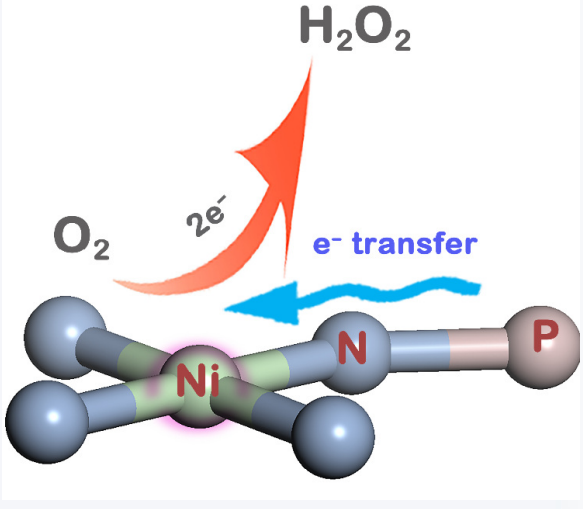

KEYWORDS: isolated metal sites, hydrogen peroxide, electrosynthesis, coordination shell modulation, oxygen reduction reaction

1 Introduction

As a valuable and environmentally friendly oxidation chemical, hydrogen peroxide (H_2O_2) has shown the diverse applications, including water treatment, pulp/textile bleaching, chemical synthesis, disinfection and also as an energy carrier [1–3]. The global H_2O_2 market value has reached approximately $5.2 billion in 2022 and the market is projected to reach 5.7 million metric tons by 2027 [4]. Currently, the industrial-scale H_2O_2 production mainly depends on the anthraquinone process (> 95%) due to the advantages such as high yield and large-scale preparation. However, multistep hydrogenation, oxidation, separation operations and complex centralized infrastructure are required in the energy-intensive anthraquinone process, with substantial organic waste generated [5, 6]. Therefore, exploring the energy-efficient process for H_2O_2 production under green and mild conditions is urgent for the H_2O_2-related industries. Electrosynthesis of H_2O_2 powered by renewable electricity provides a promising alternative to the traditional anthraquinone oxidation process [7, 8]. This method allows electrocatalytic two-electron oxygen reduction reaction (ORR) to generate H_2O_2, offering a potential and efficient route under safe, cost-effective and green conditions. Nevertheless, the electrosynthesis of H_2O_2 through the 2e$^-$ ORR is challenged by the competitive 4e$^-$ ORR pathway, restricting the catalytic selectivity for H_2O_2 production and the further large-scale application of this technology [9, 10]. Hence, the development of ORR electrocatalysts with high selectivity towards H_2O_2 generation is much desired.

In recent years, significant efforts have been dedicated to the development of H_2O_2 electrosynthesis, including the design of noble metals/alloys, transition metal-based compounds, metal-free

Received: December 3, 2024; **Revised:** December 20, 2024
Accepted: December 23, 2024

✉Address correspondence to xiaogangli@sdu.edu.cn

carbon materials and single-atom catalysts [11–15]. Remarkably, the carbon-based single-atom catalysts have received great attention due to their high atom unitization, well-order structure, and tunable coordination environment [16–19]. In particular, isolated metal sites coordinated with nitrogen (denoted as M-N_x sites) in carbon matrix present high performance in diverse catalytic applications [20–28]. And the catalytic properties of M-N_x related to the adsorption of reaction intermediates could be modulated by regulating its local environment around metal atoms. This provides a promising way to tune the adsorption of OOH*, which is the key intermediate during ORR process, to boost the oxygen reduction toward the 2e⁻ pathway. Previous studies have modified the local environment of M-N_x sites by changing the metal centers, coordinated elements and numbers in the first coordination shell, through which the adsorption of OOH* could be modulated and thus the H_2O_2 generation is favored [29–31]. It should be noted that the modification in the second coordination shell with functional elements or group can also finely tailor the electron localization around the M-N_x sites while being limited within a small range. This offers a mild but precise way to regulate the adsorption of intermediates. It is, therefore, important to investigate the modulation of single-atom sites in the second coordination shell towards the 2e⁻ ORR, which is, however, still at an early research stage.

Herein, we reported the phosphorus-modulated single Ni-N_4 sites on carbon support (NiN_4-PC, with 1.13 wt.% Ni loading) for electrosynthesis of H_2O_2, where the P (0.5 wt.%) is introduced into the second coordination shell around Ni-N_4 moiety. Synchrotron-based X-ray absorption spectroscopy (XAS) reveals the local structure of Ni-N_4 sites with neighboring P, demonstrating the introduction of P into the second coordination shell. Theoretical study together with XAS and X-ray photoelectron spectroscopy (XPS) results show the neighboring P triggers the electron redistribution around NiN_4 sites, resulting in the electron-rich central Ni sites which strengthen the OOH* adsorption and lower the energy barrier for H_2O_2 formation. The resultant NiN_4-PC gives an enhanced selectivity above 88% in a wide potential range for H_2O_2 generation during the electrocatalytic ORR process, higher than NiN_4 sites without P (denoted as NiN_4-C, with 1.25 wt.% Ni loading) with the 2e⁻ selectivity lower than 50%. Impressively, NiN_4 sites with P modulation in the second coordination shell could also achieve the Faradaic efficiency above 90% under a current density of 150 mA·cm^{-2} in a flow cell. This work demonstrates the effectiveness of modulating the second coordination shell for atomically dispersed metal moiety, offering insights for the design of the active sites towards the 2e⁻ ORR and other potential catalytic reactions.

2 Experimental

2.1 Synthesis of electrocatalysts

Synthesis of NiN_4-C. 3 g of dicyandiamide, 15 g of NH_4Cl and 0.25 mmol $NiCl_2$ were dissolved in deionized water and dried by rotary evaporation. Then, the dried powder was placed in a crucible and heated at 550 °C for 2 h in a muffle furnace to get the Ni-doped g-C_3N_4. Then 0.5 g Ni-doped g-C_3N_4 and 0.01 mol glucose were dispersed into 35 mL water under sonication for 2 h. After stirring another 2 h, the solution was transferred into a 50 mL Teflon-lined autoclave, sealed and heated at 180 °C for 10 h. The product, after the hydrothermal process, was washed with water and ethanol several times and dried at 60 °C. Then, the dried sample was annealed at 900 °C in Ar atmosphere for 1 h to get the NiN_4-C.

Synthesis of NiN_4-PC. 0.5 g Ni-doped g-C_3N_4 mentioned above and 0.01 mol glucose were dispersed into 35 mL water under sonication for 2 h. After stirring another 2 h, the solution was transferred into a 50 mL Teflon-lined autoclave, sealed and heated at 180 °C for 10 h. The product, after the hydrothermal process, was washed with water and ethanol several times and dried at 60 °C. After the hydrothermal process, 50 mg sample was taken and dispersed into ethanol with 500 mg triphenylphosphine. The solution was dried through rotary evaporation. Then, the dried sample was annealed in the tube furnace at 900 °C in Ar atmosphere for 1 h to get the NiN_4-PC.

Synthesis of N-C. The synthesis process of N-C was the same as that of NiN_4-C except for the addition of $NiCl_2$.

Synthesis of N-PC. The N-PC was prepared using a similar procedure to that of NiN_4-PC, except that Ni-doped g-C_3N_4 was replaced by g-C_3N_4 without Ni.

2.2 Materials characterization

Transmission electron microscopy (TEM) images were taken on HT-7700. The X-ray diffraction (XRD) of the as-prepared materials was explored by using a Bruker D8 Advance X-ray diffractometer with Cu Kα radiation (λ = 1.5418 Å). The sub angstrom-resolution high-angle annular dark-field scanning TEM (HAADF-STEM) characterizations were performed on a Spectra 300 with a spherical aberration corrector. The metal loading in the catalysts was determined by inductively coupled plasma-mass spectrometry (ICP-MS, NEXION350X). The ultraviolet–visible (UV–vis) absorption data were collected on T700B spectrophotometer (Beijing Purkinje General Instrument Co., Ltd.). XPS results were obtained on X-ray photoelectron spectrometer (Thermo ESCALAB 250Xi) with Al Kα ($h\nu$ = 1486.6 eV) as the excitation source. The X-ray absorption fine structure spectra were detected by BL14W1 station in Shanghai Synchrotron Radiation Facility.

2.3 Electrochemical measurements

Electrochemical tests on rotating ring-disk electrode (RRDE, AFE7R9GCPT model, Pine Instruments; disk diameter = 5.61 mm; collection efficiency: 37%) were performed by electrochemical workstation (CHI 760E) in a three-electrode configuration with Ag/AgCl electrode (filled with fresh 3 M KCl solution) as the reference electrode and carbon rod as the counter electrode. To prepare the working electrode, 4 mg sample was added into 0.96 mL isopropyl alcohol with 40 μl Nafion solution (Nafion 117) and ultrasonically mixed to get the homogeneous ink. The ink was loaded onto disk of RRDE with a loading of 0.1 mg·cm^{-2}. Linear sweep voltammetry (LSV) test was performed in O_2-saturated 0.1 M KOH solution with a scan rate of 5 mV·s^{-1} at 1600 rpm. The applied potential on Pt ring during LSV test was set as 1.2 V vs. reversible hydrogen electrode (RHE). Successive cycle voltammetry with a rapid scan rate in the potential range of 0.2–0.6 V (vs. RHE) was carried out on the Pt ring of RRDE before every LSV test to fresh the ring electrode.

3 Results and discussion

The strategy for synthesizing NiN_4-PC is shown in Fig. 1(a). The morphology of the catalysts was confirmed by TEM. Figure 1(b)

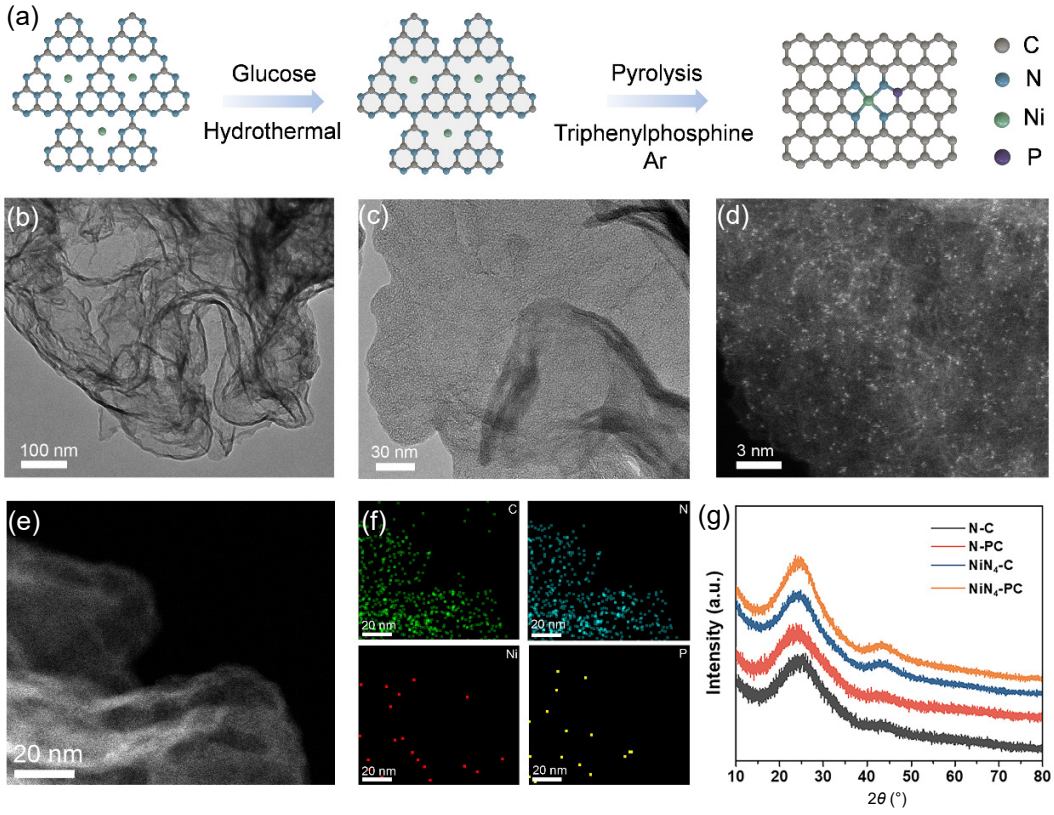

Figure 1 (a) Schematic illustration of the preparation process of NiN_4-PC. (b) TEM image of NiN_4-PC. (c) High-magnification TEM image for NiN_4-PC. (d) HAADF-STEM image for NiN_4-PC. (e) Bright field TEM image of NiN_4-PC. (f) Element mapping images of NiN_4-PC. (g) XRD patterns of the catalysts.

presents the TEM image of NiN_4-PC, which shows a sheet-like structure, similar to that of NiN_4-C, as depicted in Fig. S1(a) in the Electronic Supplementary Material (ESM). And no particles are observed from the high-magnification TEM image for NiN_4-PC and NiN_4-C, as shown in Fig. 1(c) and Fig. S1(b) in the ESM. The HAADF-STEM image for NiN_4-PC in Fig. 1(d) reveals isolated bright spots, which correspond to the Ni atoms, indicating the single-atom form of Ni in NiN_4-PC. The atomically dispersed Ni is also observed for NiN_4-C, as seen in Fig. S2 in the ESM, demonstrating the atomic configuration of Ni sites. These results indicate the introduction of phosphorus did not disrupt the isolated configuration of Ni sites. Energy-dispersive X-ray spectroscopy (EDX) mapping analysis in Figs. 1(e) and 1(f) indicate that Ni, P and N atoms distribute homogeneously in carbon substrate. The XRD patterns of the samples with N-doped carbon (denoted as N-C) and N, P-doped carbon (N-PC) as references in Fig. 1(g) show two typical broad peaks at about 24° and 44°, which could be ascribed to (002) and (101) lattice plane of graphite [32, 33]. No peaks corresponding to a metallic phase appear in the XRD patterns for NiN_4-PC and NiN_4-C, further corroborating that Ni sites are atomically dispersed.

XAS was carried out to determine to local structure of Ni sites in NiN_4-C and NiN_4-PC. Figure 2(a) presents the Ni K-edge X-ray absorption near-edge structure (XANES) curves of NiN_4-C and NiN_4-PC compared with Ni foil as the reference. It is clearly seen that the absorption edges of NiN_4-C and NiN_4-PC show a positive shift compared with that of Ni foil, indicating the higher oxidation state of Ni in NiN_4-C and NiN_4-PC than in Ni foil. In addition, the NiN_4-PC gives a slightly decreased intensity of white line peak compared with NiN_4-C, demonstrating the lower oxidation state of Ni with P modulation. The magnified pre-edge XANES spectra in Fig. S3 in the ESM also suggest the electron transfer to Ni after the P introduction, as the absorption edge position of NiN_4-PC shows a slightly negative shift compared with that of NiN_4-C. The XPS was further performed to explore this electron transfer. The high-resolution Ni 2p XPS spectra of NiN_4-C in Fig. S4 in the ESM display the binding energies of Ni $2p_{3/2}$ and Ni $2p_{1/2}$ peaks at 855.2 and 872.7 eV, respectively, with two related satellite peaks [34]. The NiN_4-PC shows the similar peaks but with a slight energy shift. Taking the deconvoluted Ni $2p_{3/2}$ peak out as a demonstration, clear negative shift in the binding energy could be observed for NiN_4-PC compared with that of NiN_4-C (Fig. 2(b)), agreed well with the XANES results, which thus confirms the electron redistribution resulted from the P modulation. In addition, the P 2p XPS result of NiN_4-PC could be deconvoluted into P–C (131.9 eV) and P–N (133.1 eV) bonds [35], respectively, as shown in Fig. S5 in the ESM. The absence of the characteristic peak of metal–P bond implies P atoms tend to bond to surrounding N atoms, not directly to the central Ni atoms. Furthermore, when compared with the N-PC without Ni, the P–N peak of NiN_4-PC presents a shift towards the higher energy, indicating the electron transfer from P to Ni through N atom, consistent with the Ni XANES and XPS results.

Figure 2(c) displays the Fourier transform of extended X-ray absorption fine structure (FT-EXAFS) spectra. The FT-EXAFS curves of NiN_4-C and NiN_4-PC only present a dominant peak for bond distances shorter than 2.0 Å, with no Ni–Ni interactions observed compared with Ni foil, indicating the atomically dispersed Ni sites in NiN_4-C and NiN_4-PC samples. The main peaks at approximately 1.5 Å for NiN_4-C and NiN_4-PC can be ascribed to the single scattering of photoelectrons excited by an X-ray from Ni

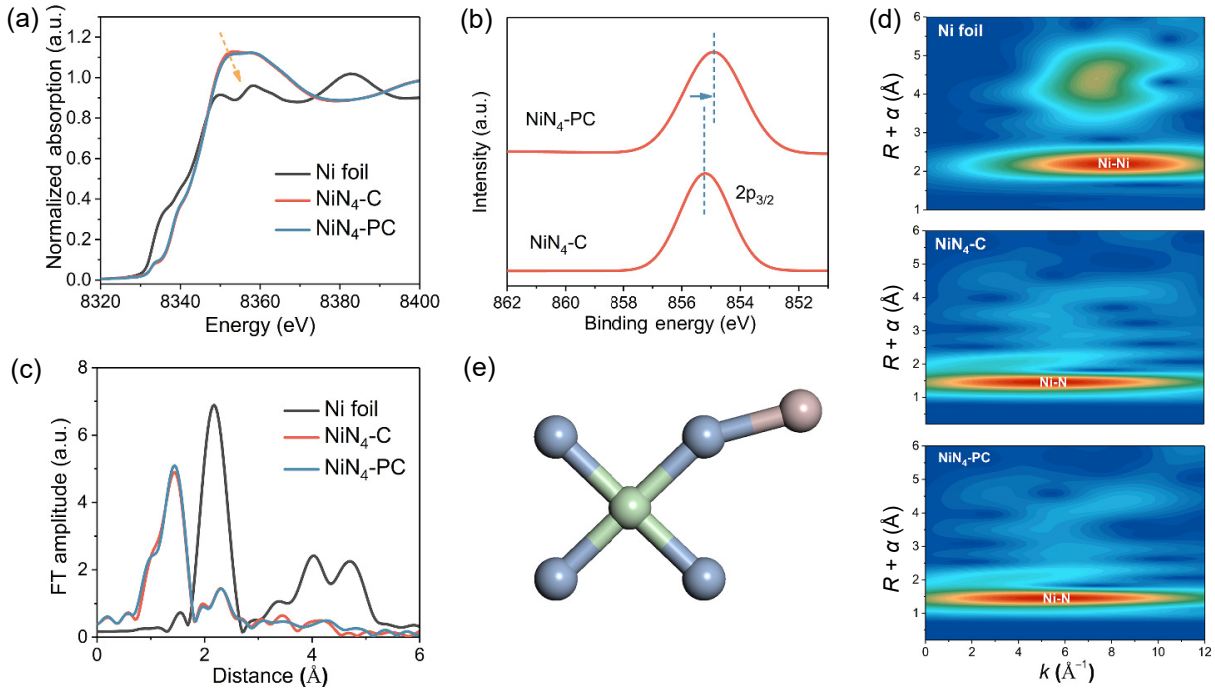

Figure 2 (a) Ni K-edge XANES curves of NiN_4-C, NiN_4-PC and Ni foil. (b) Ni $2p_{3/2}$ peak from the XPS results for NiN_4-C and NiN_4-PC. (c) FT-EXAFS spectra of NiN_4-C, NiN_4-PC and Ni foil. (d) WT-EXAFS results of NiN_4-C, NiN_4-PC and Ni foil. (e) Structural model for NiN_4-P sites.

atoms to the nearest neighbored N atoms, which forms the Ni-N shell in the first coordination shell. Considering the powerful resolution in both k and r spaces, the Ni K-edge wavelet transform (WT)-EXAFS was performed to investigate the atomic configuration of NiN_4-C and NiN_4-PC, as shown in Fig. 2(d). Ni foil shows an intensity maximum at 8.06 $Å^{-1}$ in the WT contour plots, corresponding to the metallic Ni–Ni coordination. As for NiN_4-C and NiN_4-PC, only one intensity maximum at 5.30 and 5.39 $Å^{-1}$ was observed in the WT contour plots, respectively, which could be ascribed the Ni–N coordination. The absence of the corresponding signal for the Ni–Ni interaction strongly corroborates the atomic dispersion of Ni species in these two catalysts. Quantitatively, the structural parameters at Ni K-edge for NiN_4-C and NiN_4-PC were extracted by least-square EXAFS fitting. The fitting results are shown in Fig. S6 and Table S1 in the ESM. It could be seen that the experimental FT-EXAFS curves of the NiN_4-C and NiN_4-PC have been perfectly reproduced. The fitting results show that Ni was bonded by four nitrogen atoms for both NiN_4-C and NiN_4-PC, suggesting the same Ni–N_4 coordination structure in these two samples. These results also exclude the possibility that P atom is located in the first coordinated shell of Ni sites. N 1s XPS was further performed to determine the type of the chemical bond related to Ni sites and the results are shown in Fig. S7 in the ESM. The N–C is the reference here, for which the N 1s spectra could be deconvolved into four peaks corresponding to pyridinic-N (398.15 eV), pyrrolic-N (399.45 eV), graphitic-N (400.95 eV), and oxidized-N (402.30 eV), respectively. With the introduction of NiN_4 sites, the peak corresponding to pyridinic-N in NiN_4-C shows a positive shift compared with N–C, indicating the chemical bonding between pyridinic N and Ni atoms [36]. Further introducing the P atom results in the pyridinic-N in NiN_4-PC shifting back towards the lower binding energy, suggesting the electron transfer from neighboring P in the second coordination shell to pyridinic-N in the first coordination shell, which also leads to the electron-rich central Ni atoms, as confirmed by the XANES and XPS results mentioned above. The XPS results also exclude the potential influence of Cl for the structure and catalytic performance, as Cl was not observed in Fig. S8 in the ESM. Taking the XAS and XPS analysis together, NiN_4-PC shares the same Ni–N_4 configuration with NiN_4-C in the first coordination shell, but with P atom introduced into the second coordination shell, as shown in Fig. 2(e).

Electrochemical tests show that modulation from neighboring P atom boosts ORR selectivity of NiN_4 sites toward the $2e^-$ pathway. Figure 3(a) gives the linear-sweep voltammetry (LSV) curves of NiN_4-C and NiN_4-PC. NiN_4-PC shows the increased catalytic ORR current for H_2O_2 production, as compared with NiN_4-C. Based on the disk and ring current, the selectivity for H_2O_2 generation was calculated. As shown in Fig. 3(b), NiN_4-PC delivers above 88% selectivity for the $2e^-$ ORR pathway across a wide potential range, much higher than that of NiN_4-C with the H_2O_2 selectivity less than 50%. This indicates the modulation in the second coordination hell for isolated metal sites could effectively tune the catalytic selectivity. The Brunauer–Emmett–Teller (BET) characterization also excludes the contribution from surfaces and porous structures of the catalysts to the enhanced catalytic performance, as shown in Fig. S9 in the ESM. As for the samples without the Ni sites, the introduction of P shows the limited enhancement for the catalytic selectivity towards the H_2O_2 generation, as seen in Fig. S10 in the ESM, demonstrating the isolated metal sites are more sensitive to exotic regulation. The related electron transfer number during the ORR process was also calculated to evaluate the catalytic selectivity. As shown in Fig. S11 in the ESM, NiN_4-PC presents a decreased electron transfer number that is closer to 2, compared with NiN_4-C, N-C and N-PC, further demonstrating its excellent catalytic performance for H_2O_2 production. In addition, the P-modulated NiN_4 sites deliver a higher onset potential (Table S2 in the ESM), indicating the decreased overpotential for H_2O_2 generation. The ORR selectivity was further explored based on the H_2O_2 reduction reaction. As seen in Fig. 3(c), NiN_4-PC delivered a decreased

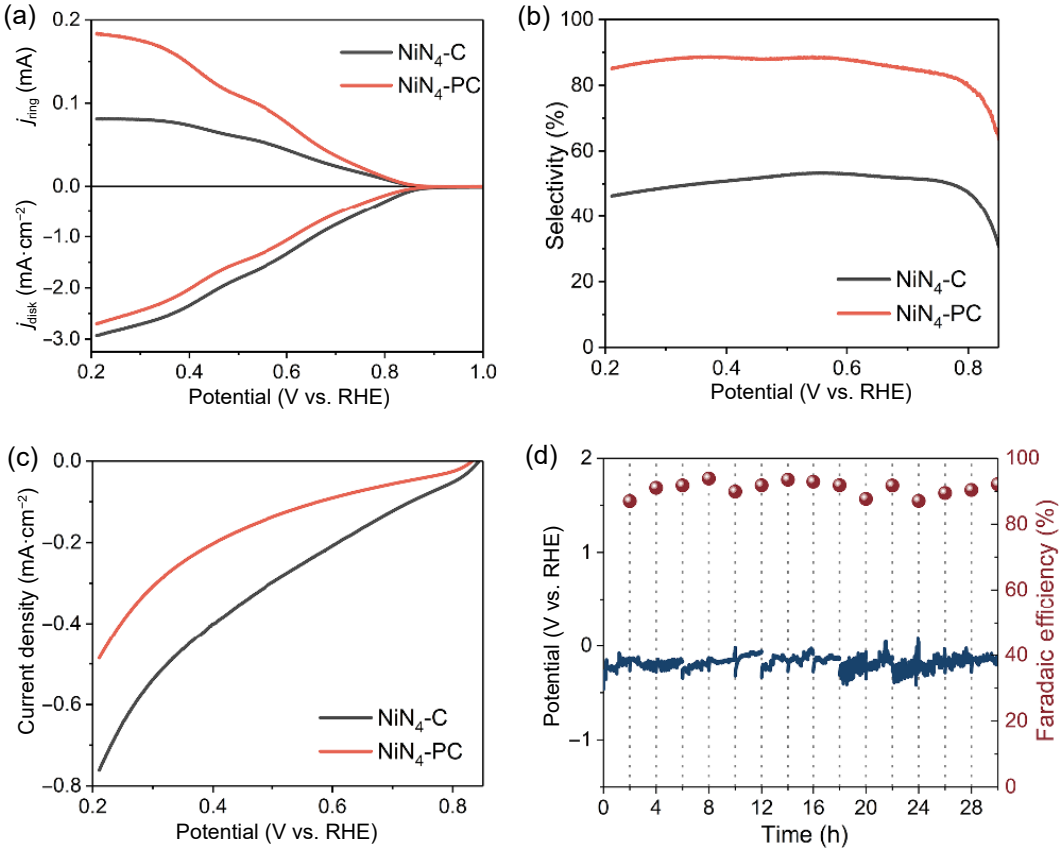

Figure 3 (a) LSV curves of the electrocatalysts on RRDE in O_2-saturated 0.1 M KOH. (b) Calculated selectivity for H_2O_2 generation. (c) LSV curves in N_2-saturated 0.1 M KOH containing 10 mM H_2O_2. (d) Stability test of the NiN_4-PC catalyst under 150 mA·cm^{-2} in 0.5 M KOH.

current density compared with NiN_4-C, indicating the P modulation endows the NiN_4 moiety with inertia for the further reduction of H_2O_2, agreed well with the excellent selectivity of NiN_4-PC for the 2e$^-$ ORR pathway. To confirm the Ni other than P atom as the catalytic sites, the SCN^-, a commonly adopted ion to poison metal sites [37], was used as the indicator for active sites. As seen in Fig. S12 in the ESM, clear depression of catalytic current for NiN_4-PC is observed, which could be ascribed to the blocking of Ni atoms by SCN^-, thus confirming Ni atoms as the catalytic center. The catalytic stability and related Faradaic efficiency for producing H_2O_2 were then investigated. The $Ce(SO_4)_2$ titration method was used to determine the amount of generated H_2O_2 [38]. The UV absorbance of $Ce(SO_4)_2$ solution related concentration and corresponding calibration curve are shown in Fig. S13 in the ESM. Based on this $Ce(SO_4)_2$ titration method, the amount of generated H_2O_2 and related Faradaic efficiency during the ORR process could be calculated. Figure S14 in the ESM presents the amperometric test (current–time, *I*–*t*) results and Faradaic efficiency for generating H_2O_2. The NiN_4-PC shows a high Faradaic efficiency at 0.5 V during two 24-h cycle tests with a relatively stable current density, indicating its excellent catalytic selectivity and stability. We further investigated the H_2O_2 production capacity of NiN_4-PC on a gas diffusion electrode in flow cell. As seen in Fig. 3(d), under the current density of 150 mA·cm^{-2}, NiN_4-PC displays a high Faradaic efficiency of up to 93.1%, with negligible activity loss over 30-h test. Impressively, the average H_2O_2 production yield rate reaches 5.08 mmol per 2 h (Fig. S15 in the ESM), corresponding to 5.08 mol·g_{cat}^{-1}·h^{-1}, demonstrating the superiority of NiN_4-PC towards electrosynthesis of H_2O_2.

To better understand the modulation of neighboring P on Ni-N_4 sites for the ORR process, density functional theory (DFT) calculations are performed to shed light on the origin of observed pathway regulation (see computational details and Table S3 in the ESM). Figure S16(a) in the ESM depicts the optimized structures of NiN_4-C and NiN_4-PC. The calculated formation energy for NiN_4-PC shows a thermodynamically favorable value of −1.80 eV, suggesting its structural stability. The charge difference state and Bader charge were carried out to reveal the changes for Ni atom valance, as shown in Fig. S16(b) in the ESM, in which the values of the NiN_4-C and NiN_4-PC were calculated to be 0.844 and 0.838, respectively. The results indicate that the neighboring P atom located at second coordination shell could regulate the electronic structure of central Ni atom, leading to the tunable interaction of ORR intermediates with active sites. Compared with NiN_4-C, the NiN_4-PC shows the favorable O_2 adsorption but with same length of O–O bond, as shown in Fig. S17 in the ESM, which hinders the cleavage of the O–O bond and facilitates the 2e$^-$ pathway of ORR. The free energy diagrams depicted in Fig. 4(a) illustrate the OOH* formation is thermodynamically favored after the P modulation. NiN_4-PC shows the significantly decreased energy barrier of 0.14 eV, compared with NiN_4-C with the energy barrier of 0.65 eV, indicating the improved 2e$^-$ ORR activity on P modified Ni-N_4 sites. As the reliable ORR descriptor, the binding strength of *OOH was further used to construct thermodynamic limiting potential (U_L) volcano plot [39, 40], which could signify the catalytic ORR activity and selectivity. The CoN_4 and FeN_4 sites are also summarized here to give a better presentation for the volcano plots. As shown in Fig. 4(b), the NiN_4-C is located on the right leg of

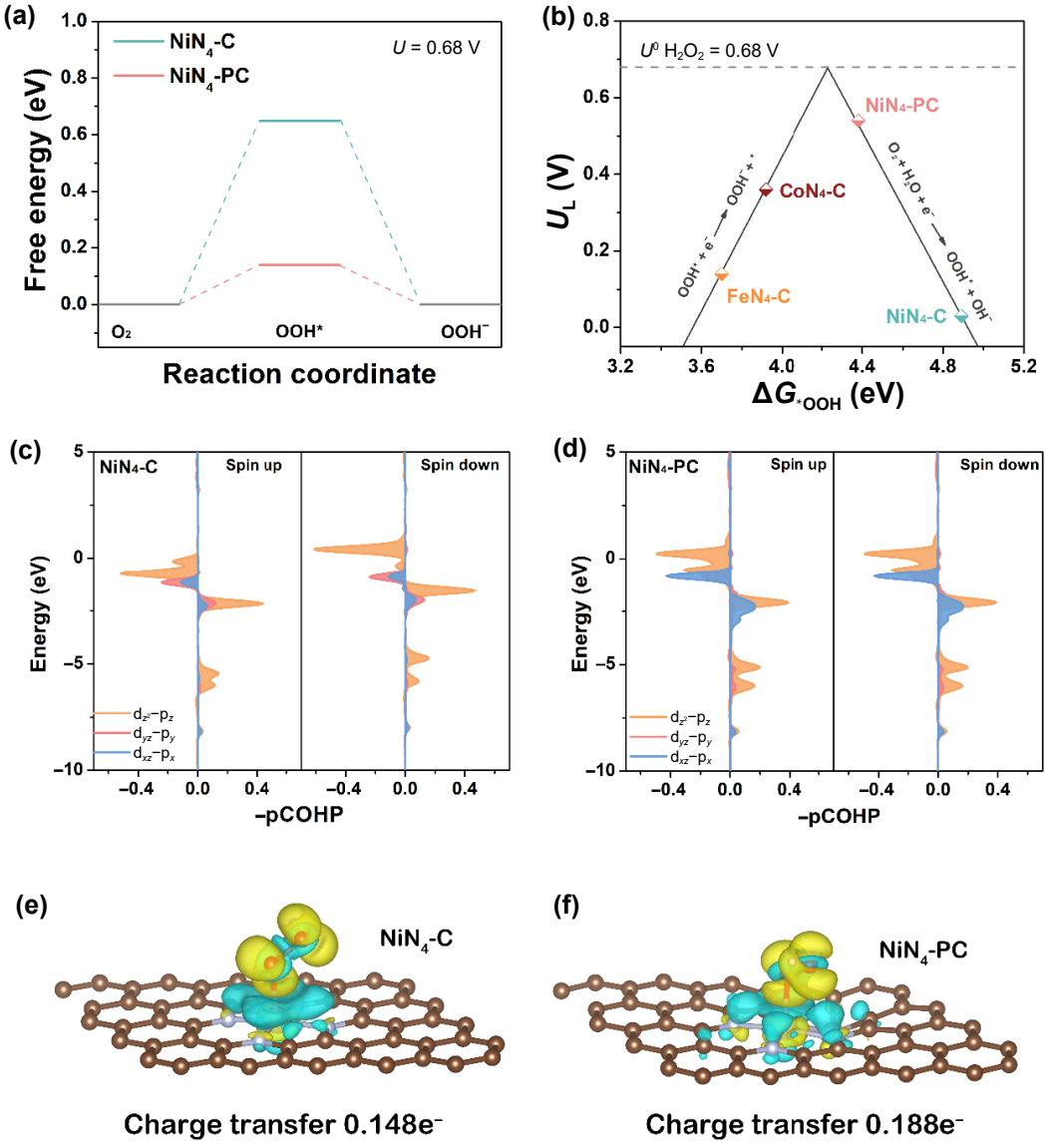

Figure 4 (a) Free-energy diagrams for 2e⁻ ORR pathway at 0.68 V vs. RHE. (b) Calculated activity-volcano plots for 2e⁻ ORR. (c) pCOHPs between Ni and p-orbital of O of *OOH on NiN_4-C. (d) pCOHPs between Ni and p-orbital of O of *OOH on NiN_4-PC. (e) Bader charge density difference of NiN_4-C after *OOH adsorbed. (f) Bader charge density difference of NiN_4-PC after *OOH adsorbed. Cyan and yellow isosurfaces represent electron loss and electron gain, respectively.

volcano plots, where *OOH formation is the potential limiting step. This binding energy here implies the further dissociation *OOH is suppressed but with a larger overpotential for H_2O_2 generation. With the P atom embedded into the second coordination shell, NiN_4-PC gives the Gibbs free energy (ΔG_{*OOH}) value of 4.38 eV, shifting leftward on the volcano plots towards the apex compared with NiN_4-C, demonstrating the enhanced activity and selectivity towards the 2e⁻ ORR. To further unravel the interaction of Ni sites with the adsorbed *OOH, we then investigated the projected density of states (PDOS) for NiN_4-C and NiN_4-PC (Fig. S18 in the ESM). The NiN_4-C with adsorbed *OOH displays the spin-polarized PDOS that is mainly contributed by d_{z^2} and d_{yz} coupled with p_z and p_y, respectively, while NiN_4-PC shows symmetric states composed of d_{z^2}, d_{xz} and d_{yz} coupled with p_z, p_x and p_y. The difference of orbital hybridization about NiN_4-C and NiN_4-PC will give a distinguishing interaction of Ni sites with *OOH [41]. The projected crystal orbital Hamilton population (pCOHP) analysis was employed to further explain the bond strength between the Ni atom and the O atom from *OOH [42]. The pCOHP of NiN_4-C in Fig. 4(c) shows that the $d_{z^2}-p_z$ antibonding orbitals of spin down state are located at unoccupied states, while the $d_{z^2}-p_z$ antibonding orbitals of spin up state are almost fully occupied, which contributes to a weaker *OOH adsorption. In contrast, pCOHP of NiN_4-PC in Fig. 4(d) reveals that a large proportion of $d_{z^2}-p_z$ antibonding orbitals for both spin states is unoccupied, which leads to enhanced *OOH adsorption. The reinforced Ni–O interaction was also verified by integrated COHP (iCOHP) below Fermi level (Fig. S19 in the ESM) [43]. The NiN_4-PC display more negative iCOHP value of both spin states (spin up: −0.75; spin down: −0.75) compared with that of NiN_4-C (spin up: −0.30 spin down: −0.67). Charge density difference and Bader charge analysis between Ni sites and *OOH intermediate are shown in Figs. 4(e) and 4(f), in which the electron transfer from Ni site to O atom with the adsorbed *OOH intermediate could be observed. The neighboring P induces the enhanced electron transfer (0.188e⁻) compared with that (0.148e⁻) without P modulation, illustrating the strengthened

Ni–O interaction between the Ni sites and *OOH with P introduction, thus decreasing the energy barrier for H_2O_2 generation. The above calculation results indicate that the introduction of P in second coordination sphere could contribute to the enhanced activity and selectivity of the NiN_4 sites towards the $2e^-$ ORR reaction, consistent with the experimental observations.

4 Conclusions

In conclusion, we demonstrated a phosphorus modulation strategy for isolated Ni-N_4 sites towards the electrocatalysis of H_2O_2. The P atom is embedded into the second coordination shell of Ni-N_4 sites, triggering the tunable adsorption of *OOH and thus boosting the electrocatalytic ORR through the $2e^-$ pathway. The P modified Ni-N_4 sites deliver an enhanced selectivity near 90% for H_2O_2 generation with decreased overpotential compared with that of bare Ni-N_4 sites, indicating the effective regulation of local coordination environment around central Ni atoms. DFT calculations combined with XAS and XPS techniques demonstrate the electron transfer to Ni atom, leading to the enhanced *OOH adsorption, favoring the $2e^-$ reduction of O_2 to H_2O_2. We anticipate this work would provide a promising approach to modulate the second coordination shell of single-atom catalysts and pave a new avenue for rationally designing high-efficiency catalysts.

Electronic Supplementary Material: Supplementary material (additional characterization results) is available in the online version of this article at https://doi.org/10.26599/NR.2025.94907211.

Data availability

All data needed to support the conclusions in the paper are presented in the manuscript and the Electronic Supplementary Material. Additional data related to this paper may be requested from the corresponding author upon request.

Acknowledgements

This work was financially supported by the Taishan Scholar Project Foundation of Shandong Province (Nos. tsqn202211028 and tsqn202306080), the Natural Science Foundation of Shandong Province (Nos. ZR2022JQ08 and 2023HWYQ-028), and the Instrument Improvement Founds of Shandong University Public Technology Platform (No. ts20230209).

Declaration of competing interest

All the contributing authors report no conflict of interests in this work.

Author contribution statement

H. Z.: Data curation, analysis, writing – original draft, writing – review & editing. N. Z.: Data curation, analysis, B. J. X.: Writing – review & editing. F. W.: Data curation, analysis. K. P. S.: Data curation, analysis. X. G. A.: Data curation, analysis. S. L. X.: Funding acquisition, resources, writing – review & editing. X. G. L.: Funding acquisition, resources, supervision. All the authors have approved the final manuscript.

Use of AI statement

None.

References

[1] Wang, M. J.; Dong, X.; Meng, Z. D.; Hu, Z. W.; Lin, Y. G.; Peng, C. K.; Wang, H. S.; Pao, C. W.; Ding, S. Y.; Li, Y. Y. et al. An efficient interfacial synthesis of two-dimensional metal-organic framework nanosheets for electrochemical hydrogen peroxide production. *Angew. Chem., Int. Ed.* **2021**, *60*, 11190–11195.

[2] Chen, H.; He, C. H.; Niu, H. T.; Xia, C. F.; Li, F. M.; Zhao, W. S.; Song, F.; Yao, T.; Chen, Y.; Su, Y. Q. et al. Surface redox chemistry regulates the reaction microenvironment for efficient hydrogen peroxide generation. *J. Am. Chem. Soc.* **2024**, *146*, 15356–15365.

[3] Fan, W. J.; Duan, Z. Y.; Liu, W.; Mehmood, R.; Qu, J. T.; Cao, Y. C.; Guo, X. Y.; Zhong, J.; Zhang, F. X. Rational design of heterogenized molecular phthalocyanine hybrid single-atom electrocatalyst towards two-electron oxygen reduction. *Nat. Commun.* **2023**, *14*, 1426.

[4] Qi, D. F.; Xu, J.; Zhou, Y. T.; Zhang, H.; Shi, J. Q.; He, K.; Yuan, Y. F.; Luo, J.; Wang, S.; Wang, Y. Cyclodextrin-supported $Co(OH)_2$ clusters as electrocatalysts for efficient and selective H_2O_2 synthesis. *Angew. Chem., Int. Ed.* **2023**, *62*, e202307355.

[5] Xu, S. R.; Yu, Y.; Zhang, X. Y.; Xue, D. P.; Wei, Y. F.; Xia, H. C.; Zhang, F. X.; Zhang, J. N. Enhanced electron delocalization induced by ferromagnetic sulfur doped C_3N_4 triggers selective H_2O_2 production. *Angew. Chem., Int. Ed.* **2024**, *63*, e202407578.

[6] Li, X. G.; Xu, W. J.; Le, L. Q.; Chen, S. M.; Song, L.; Choksi, T. S.; Wang, X. Sulfur-modulated isolated NiN_x sites toward electrocatalytic hydrogen peroxide generation. *Chem Catal.* **2023**, *3*, 100724.

[7] Zhang, X. L.; Su, X. Z.; Zheng, Y. R.; Hu, S. J.; Shi, L.; Gao, F. Y.; Yang, P. P.; Niu, Z. Z.; Wu, Z. Z.; Qin, S. et al. Strongly coupled cobalt diselenide monolayers for selective electrocatalytic oxygen reduction to H_2O_2 under acidic conditions. *Angew. Chem., Int. Ed.* **2021**, *60*, 26922–26931.

[8] Xia, C.; Kim, J. Y. Wang, H. T. Recommended practice to report selectivity in electrochemical synthesis of H_2O_2. *Nat. Catal.* **2020**, *3*, 605–607.

[9] Liu, L. X.; Kang, L. Q.; Feng, J. R.; Hopkinson, D. G.; Allen, C. S.; Tan, Y. S.; Gu, H.; Mikulska, I.; Celorrio, V.; Gianolio, D. et al. Atomically dispersed asymmetric cobalt electrocatalyst for efficient hydrogen peroxide production in neutral media. *Nat. Commun.* **2024**, *15*, 4079.

[10] Wei, G. Y.; Li, Y. X.; Liu, X. P.; Huang, J. R.; Liu, M. R.; Luan, D. Y.; Gao, S. Y.; Lou, X. W. Single-atom zinc sites with synergetic multiple coordination shells for electrochemical H_2O_2 production. *Angew. Chem., Int. Ed.* **2023**, *62*, e202313914.

[11] Jiang, Y. Y.; Ni, P. J.; Chen, C. X.; Lu, Y. Z.; Yang, P.; Kong, B.; Fisher, A.; Wang, X. Selective electrochemical H_2O_2 production through two-electron oxygen electrochemistry. *Adv. Energy Mater.* **2018**, *8*, 1801909.

[12] Li, H.; Wen, P.; Itanze, D. S.; Hood, Z. D.; Adhikari, S.; Lu, C.; Ma, X.; Dun, C. C.; Jiang, L.; Carroll, D. L. et al. Scalable neutral H_2O_2 electrosynthesis by platinum diphosphide nanocrystals by regulating oxygen reduction reaction pathways. *Nat. Commun.* **2020**, *11*, 3928.

[13] Wu, K. H.; Wang, D.; Lu, X. Y.; Zhang, X. F.; Xie, Z. L.; Liu, Y. F.; Su, B. J.; Chen, J. M.; Su, D. S.; Qi, W. et al. Highly selective hydrogen peroxide electrosynthesis on carbon: *In situ* interface engineering with surfactants. *Chem* **2020**, *6*, 1443–1458.

[14] Zhang, Y.; Lyu, Z.; Chen, Z. T.; Zhu, S. Q.; Shi, Y. F.; Chen, R. H.; Xie, M. H.; Yao, Y.; Chi, M. F.; Shao, M. H. et al. Maximizing the catalytic performance of $Pd@AuxPd_{1-x}$ nanocubes in H_2O_2 production by reducing shell thickness to increase compositional stability. *Angew. Chem., Int. Ed.* **2021**, *60*, 19643–19647.

[15] Zhuang, Z. W.; Huang, A. J.; Tan, X.; Sun, K. A.; Chen, C.; Peng, Q.;

Zhuang, Z. B.; Han, T.; Xiao, H.; Zeng, Y. et al. p-Block-metal bismuth-based electrocatalysts featuring tunable selectivity for high-performance oxygen reduction reaction. *Joule* **2023**, *7*, 1003–1015.

[16] Ji, S. F.; Chen, Y. J.; Wang, X. L.; Zhang, Z. D.; Wang, D. S.; Li, Y. D. Chemical synthesis of single atomic site catalysts. *Chem. Rev.* **2020**, *120*, 11900–11955.

[17] Li, X. G.; Tang, S. S.; Dou, S.; Fan, H. J.; Choksi, T. S.; Wang, X. Molecule confined isolated metal sites enable the electrocatalytic synthesis of hydrogen peroxide. *Adv. Mater.* **2022**, *34*, 2104891.

[18] Liu, S. W.; Li, C. Z.; Zachman, M. J.; Zeng, Y. C.; Yu, H. R.; Li, B. Y.; Wang, M. Y.; Braaten, J.; Liu, J. W.; Meyer, H. M. et al. Atomically dispersed iron sites with a nitrogen-carbon coating as highly active and durable oxygen reduction catalysts for fuel cells. *Nat. Energy* **2022**, *7*, 652–663.

[19] Sun, J. Q.; Tao, L.; Ye, C. L.; Wang, Y.; Meng, G.; Lei, H. Y.; Zheng, S. K.; Xing, C.; Tao, X.; Wu, P. F. et al. MOF-derived Ru_1Zr_1/Co dual-atomic-site catalyst with promoted performance for Fischer-Tropsch synthesis. *J. Am. Chem. Soc.* **2023**, *145*, 7113–7122.

[20] Zhao, J.; Guo, Y.; Zhang, Z. Q.; Zhang, X. L.; Ji, Q. Q.; Zhang, H.; Song, Z. Q.; Liu, D. Q.; Zeng, J. R.; Chuang, C. H. et al. Out-of-plane coordination of iridium single atoms with organic molecules and cobalt-iron hydroxides to boost oxygen evolution reaction. *Nat. Nanotechnol*., in press, DOI: 10.1038/s41565-024-01807-x.

[21] Li, X. G.; Bi, W. T.; Chen, M. L.; Sun, Y. X.; Ju, H. X.; Yan, W. S.; Zhu, J. F.; Wu, X. J.; Chu, W. S.; Wu, C. Z. et al. Exclusive Ni–N_4 sites realize near-unity CO selectivity for electrochemical CO_2 reduction. *J. Am. Chem. Soc.* **2017**, *139*, 14889–14892.

[22] Najam, T.; Shah, S. S. A.; Yin, H. Q.; Xiao, X.; Talib, S.; Ji, Q. Q.; Deng, Y. G.; Javed, M. S.; Hu, J.; Zhao, R. et al. Second-shell modulation on porphyrin-like Pt single atom catalysts for boosting oxygen reduction reaction. *Chem. Sci.* **2024**, *15*, 18513–18523.

[23] Najam, T.; Shah, S. S. A.; Javed, M. S.; Chen, P. T.; Chuang, C.; Saad, A.; Song, Z. Q.; Liu, Wei.; Cai, X. K. Modulating the electronic structure of zinc single atom catalyst by P/N coordination and Co_2P supports for efficient oxygen reduction in Zn-air battery. *Chem. Eng. J.* **2022**, *440*, 135928.

[24] Najam, T.; Shah, S. S. A.; Ibraheem, S.; Cai, X. K.; Hussain, E.; Suleman, S.; Javed, M. S.; Tsiakaras, P. Single-atom catalysis for zinc-air/O_2 batteries, water electrolyzers and fuel cells applications. *Energy Storage Mater.* **2022**, *45*, 504–540.

[25] Miao, K. H.; Qin, J. D.; Yang, J.; Kang, X. W. Synergy of Ni nanoclusters and single atom site: Size effect on the performance of electrochemical CO_2 reduction reaction and rechargeable Zn–CO_2 batteries. *Adv. Funct. Mater.* **2024**, *34*, 2316824.

[26] Miao, K. H.; Qin, J. D.; Lai, S. Y.; Luo, M.; Kuchkaev, A.; Yakhvarov, D.; Kang, X. W. Spin regulation of nickel single atom catalyst via axial phosphor-coordination achieves near unity CO selectivity in electrochemical CO_2 reduction. *Adv. Funct. Mater*., in press, DOI: 10.1002/adfm.202419989.

[27] Zhao, C. X.; Liu, J. N.; Yao, N.; Wang, J.; Ren, D.; Chen, X.; Li, B. Q.; Zhang, Q. Can aqueous zinc-air batteries work at sub-zero temperatures. *Angew. Chem., Int. Ed.* **2021**, *60*, 15281–15285.

[28] Sun, Z. Y.; Li, C.; Wei, Z. H.; Zhang, F.; Deng, Z. W.; Zhou, K. J.; Wang, Y.; Guo, J. H.; Yang, J. Y.; Xiang, Z. Q. et al. Sulfur-bridged asymmetric cuni bimetallic atom sites for CO_2 reduction with high efficiency. *Adv. Mater.* **2024**, *36*, 2404665.

[29] Tang, C.; Chen, L.; Li, H. J.; Li, L. Q.; Jiao, Y.; Zheng, Y.; Xu, H. L.; Davey, K.; Qiao, S. Z. Tailoring acidic oxygen reduction selectivity on single-atom catalysts via modification of first and second coordination spheres. *J. Am. Chem. Soc.* **2021**, *143*, 7819–7827.

[30] Chen, S. Y.; Luo, T.; Li, X. Q.; Chen, K. J.; Fu, J. W.; Liu, K.; Cai, C.; Wang, Q. Y.; Li, H. M.; Chen, Y. et al. Identification of the highly active Co–N_4 coordination motif for selective oxygen reduction to hydrogen peroxide. *J. Am. Chem. Soc.* **2022**, *144*, 14505–14516.

[31] Li, Y.; Chen, J. X.; Ji, Y. X.; Zhao, Z. L.; Cui, W. J.; Sang, X. H.; Cheng, Y.; Yang, B.; Li, Z. J.; Zhang, Q. H. et al. Single-atom iron catalyst with biomimetic active center to accelerate proton spillover for medical-level electrosynthesis of H_2O_2 disinfectant. *Angew. Chem., Int. Ed.* **2023**, *62*, e202306491.

[32] Miao, K. H.; Wen, J. B.; Luo, M.; Xiang, D.; Jiang, Y. W.; Duan, D. L.; Jiang, Z.; Sun, W. M.; Mei, B. B.; Xiong, Y. J. et al. Phosphorus coordination in second shell of single-atom Cu catalyst toward acetate production in CO electroreduction. *Nano Lett.* **2024**, *24*, 12849–12856.

[33] Li, Y. Q.; Luo, X.; Wei, Z. H.; Zhang, F.; Sun, Z. Y.; Deng, Z. W.; Zhan, Z. H.; Zhao, C. F.; Sun, Q.; Zhang, L. et al. Precisely constructing charge-asymmetric dual-atom Fe sites supported on hollow porous carbon spheres for efficient oxygen reduction. *Energy Environ. Sci.* **2024**, *17*, 4646–4657.

[34] Hou, M. Y.; Zheng, L. R.; Zhao, D.; Tan, X.; Feng, W. Y.; Fu, J. T.; Wei, T. X.; Cao, M. H.; Zhang, J. T.; Chen, C. Microenvironment reconstitution of highly active Ni single atoms on oxygen-incorporated Mo_2C for water splitting. *Nat. Commun.* **2024**, *15*, 1342.

[35] Li, J. C.; Li, M.; An, N.; Zhang, S.; Song, Q. N.; Yang, Y. L.; Li, J.; Liu, X. Boosted ammonium production by single cobalt atom catalysts with high Faradic efficiencies. *Proc. Natl. Acad. Sci. USA* **2022**, *119*, e2123450119.

[36] Kamiya, K.; Kamai, R.; Hashimoto, K.; Nakanishi, S. Platinum-modified covalent triazine frameworks hybridized with carbon nanoparticles as methanol-tolerant oxygen reduction electrocatalysts. *Nat. Commun.* **2014**, *5*, 5040.

[37] Rong, X.; Wang, H. J.; Lu, X. L.; Si, R.; Lu, T. B. Controlled synthesis of a vacancy-defect single-atom catalyst for boosting CO_2 electroreduction. *Angew. Chem., Int. Ed.* **2020**, *59*, 1961–1965.

[38] Gao, J. J.; Yang, H. B.; Huang, X.; Hung, S. F.; Cai, W. Z.; Jia, C. M.; Miao, S.; Chen, H. M.; Yang, X. F.; Huang, Y. Q. et al. Enabling direct H_2O_2 production in acidic media through rational design of transition metal single atom catalyst. *Chem* **2020**, *6*, 658–674.

[39] Chen, S. C.; Chen, Z. H.; Siahrostami, S.; Kim, T. R.; Nordlund, D.; Sokaras, D.; Nowak, S.; To, J. W. F.; Higgins, D.; Sinclair, R. et al. Defective carbon-based materials for the electrochemical synthesis of hydrogen peroxide. *ACS Sustain. Chem. Eng.* **2018**, *6*, 311–317.

[40] Kulkarni, A.; Siahrostami, S.; Patel, A.; Nørskov, J. K. Understanding catalytic activity trends in the oxygen reduction reaction. *Chem. Rev.* **2018**, *118*, 2302–2312.

[41] Cao, P. K.; Quan, X.; Nie, X. W.; Zhao, K.; Liu, Y. M.; Chen, S.; Yu, H. T.; Chen, J. G. Metal single-site catalyst design for electrocatalytic production of hydrogen peroxide at industrial-relevant currents. *Nat. Commun.* **2023**, *14*, 172.

[42] Du, J. N.; Han, G. K.; Zhang, W.; Li, L. F.; Yan, Y. Q.; Shi, Y. X.; Zhang, X.; Geng, L.; Wang, Z. J.; Xiong, Y. P. et al. CoIn dual-atom catalyst for hydrogen peroxide production via oxygen reduction reaction in acid. *Nat. Commun.* **2023**, *14*, 4766.

[43] Dai, Y. K.; Liu, B.; Zhang, Z. Y.; Guo, P.; Liu, C.; Zhang, Y. L.; Zhao, L.; Wang, Z. B. Tailoring the d-orbital splitting manner of single atomic sites for enhanced oxygen reduction. *Adv. Mater.* **2023**, *35*, 2210757.